Delta doping of III–V compound semiconductors: Fundamentals and device applications

E. F. Schubert
AT&T Bell Laboratories, 600 Mountain Avenue, Murray Hill, New Jersey 07974

(Received 7 December 1989; accepted 29 January 1990)

Delta-function-like doping profiles can be obtained in semiconductors by growth-interrupted impurity deposition during molecular-beam epitaxy. The spatial localization of dopants is assessed by the capacitance–voltage profiling technique and secondary ion mass spectroscopy which yield profile widths of 20 and 37 Å for Be δ-doped GaAs grown at 500 °C, respectively. The diffusion coefficients of Si, Be, and C in GaAs and of Si in $Al_xGa_{1-x}As$ are determined and diffusion is shown to be negligible at low growth temperatures. At elevated growth temperatures, dopant redistribution occurs during epitaxial growth. The redistribution is shown to be due to (i) diffusion of dopants and (ii) Fermi-level pinning induced segregation of dopants along the growth axis. Fermi-level pinning induced segregation of dopants is a novel mechanism which results in a redistribution of dopants predominantly toward the growing surface due to electrostatic attraction of dopants and carriers localized in surface states. This mechamism is shown to be relavant at elevated growth temperatures of $\geqslant$600 °C. Electronic devices such as homostructure and heterostructure field-effect transistors which employ the δ-doping technique have a number of advantages including (i) high carrier density, (ii) proximity between electron channel and gate electrode, (iii) large breakdown voltage of the gate, and (iv) reduced short-channel effects. In addition, high transconductances are obtained in such δ-doped field-effect transistors. The optical properties of doping superlattices are significantly improved using the δ-doping technique. Quantum-confined interband transitions in doping superlattices are observed for the first time in such improved doping superlattices. Furthermore, a tunable doping superlattice laser is demonstrated, which has a tuning range of 35 Å. The tunable doping superlattice laser has a potential tuning range of 220 Å and is a candidate for a tunable source in future optical communication systems.

I. INTRODUCTION

The miniaturization of the spatial dimensions of semiconductor devices and integrated circuits is motivated by increased speed, reduced power consumption, and higher functional density. Among the limits of the down scaling of semiconductor devices are those set by materials science, growth, and processing. In addition, more fundamental physical limits, which are almost exclusively in the quantum regime, represent boundaries of the scaling process. It is a vital, important part of present and future semiconductor research to advance materials science in order to reduce spatial dimensions of semiconductor structures and, at the same time, to realize and understand the physical mechanisms which impose fundamental limits on further scaling.

This publication is devoted to the electronic, optical, and structural properties of doping distributions in semiconductors which are scaled down in one dimension to their ultimate spatial limit. This limit is reached, if the dopants are confined to a single or few monolayers of the semiconductor lattice. The thickness of the doped region is comparable to the lattice constant, i.e., only few angstroms thick. The doping distribution is then narrower than other relevant length scales, most importantly the free carrier de Broglie wavelength. Such narrow doping profiles can be mathematically described by Dirac's delta function. Semiconductors with such dopant distributions will be referred to as δ-doped semiconductors.

Delta-doped semiconductors can be grown by molecular-beam epitaxy (MBE) by suspension the regular crystal growth and evaporation of impurities on the nongrowing crystal surface. The essential components of an MBE system are shown in Fig. 1(a) and comprise resistively heated effusion cells equipped with shutters, the rotating GaAs substrate, and a high energy electron gun for surface analysis. The epitaxial growth is interrupted by closing the group-III element effusion cell and maintaining the group-V element flux thus providing an anion stabalized surface. The growth suspension typcially lasts between several seconds and several minutes. The growth suspension time is calculated according to

$$\tau = N^{2D}/Nv_g, \quad (1)$$

where N^{2D} is the desired two-dimensional density of dopants, N is the three-dimensional dopant concentration obtained at a specific effusion cell temperature, and a growth rate v_g. After growth suspension, epitaxial growth is resumed. Dopants are confined to a single atomic plane, if impurity diffusion and other broadening mechanisms are negligible and if the epitaxial crystal is atomically flat (i.e., contains no steps). This situation is shown in Fig. 1(b), where beryllium atoms are confined to the Ga plane of a GaAs lattice.

The first report of such a growth-interrupted dopant deposition is due to Bass,[1] who found that a strong surface

 © 1990 American Vacuum Society

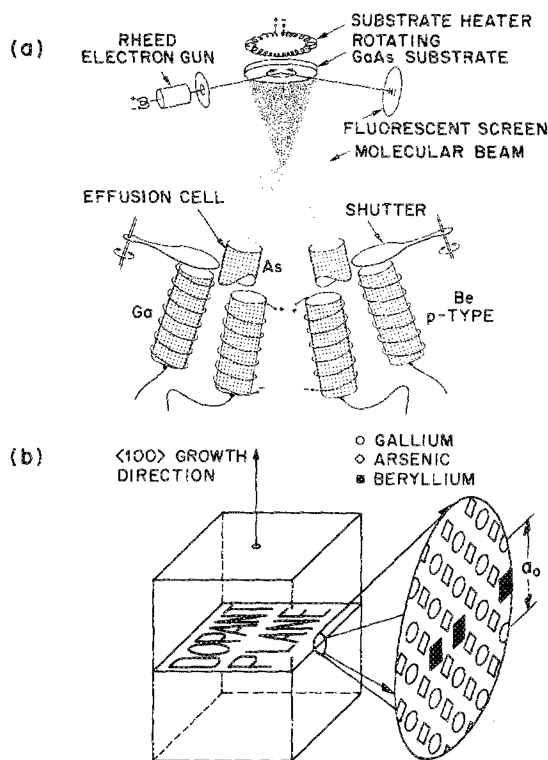

FIG. 1. (a) Schematic illustration of a molecular-beam epitaxy system comprising effusion cells with thermocouples and heating coils, shutters and a rotating substrate with heater. Also shown is a reflection high-energy electron diffraction (RHEED) gun with fluorescent screen. (b) Schematic illustration of a semiconductor grown along the ⟨100⟩ direction containing Be impurities in a single Ga plane of the GaAs zincblende structure.

adsorption of Si to the nongrowing GaAs surface results in sharp doping spikes. The width of the doping spikes is not explicitly mentioned in this publication; however, a doping profile shown in the publication reveals a width of approximately 250 Å. Adsorption of dopants to the nongrowing crystal surface may also be the origin of high dopant concentrations of the substrate–epilayer interface found earlier by DiLorenzo.[2]

The versatility of growth-interrupted dopant deposition was realized by Wood *et al.*,[3] who mentioned that complex doping profiles can be achieved by "atomic plane" or δ doping. They further found that Ge doping of GaAs leads to reduced autocompensation. However, the publication does not investigate possible diffusion of dopants from the atomic plane. Clear indications of such diffusion in δ-doped semiconductors were first found by Lee *et al.*[4] They concluded that diffusion over 126 Å occurred during crystal growth.

It was not until 1988 that Schubert *et al.*[5] showed that highly spatially confined Si doping profiles in GaAs can be achieved at substrate temperatures $\leqslant 550$ °C during growth. They concluded that Si dopants are spatially confined to a layer whose thickness is comparable to the lattice constant. They excluded diffusion over more than two lattice constants. A high degree of spatial localization was also found for Si in $Al_xGa_{1-x}As$[6] and Be in GaAs.[7] The techniques used to assess the degree of spatial localization were the capacitance–voltage profiling technique and secondary ion mass spectroscopy measurements. Both techniques were shown to be in agreement. The result of strong spatial localization of dopants in δ-doped GaAs and $Al_xGa_{1-x}As$ and the requirement of low substrate temperatures was confirmed by Santos *et al.*[8] and Webb.[9]

Novel, improved semiconductors devices were fabricated from δ-doped structures. The δ-doped metal–semiconductor field effect transistor (MESFET)[10] has the advantages of narrow channel-to-gate distance, high transconductance, and an enhanced breakdown voltage as compared to the homogeneously doped MESFET. Application of δ doping in selectively doped $Al_xGa_{1-x}As$/GaAs heterostructures[11] results in high electron densities exceeding 1×10^{12} cm^{-2}. At low temperatures the population of the ground-state subband and of the first excited subband were observed for the first time in the $Al_xGa_{1-x}As$/GaAs heterostructure system. High-transconductance selectively δ-doped heterostructure transistors exhibit superior characteristics over conventionally doped transistors.[11] Other interesting employments of the δ-doping technique include the planar-doped barrier diode,[12] mixer diodes,[13] unipolar light-emitting superlattice structures,[14] and negative differential conductance oscillators.[15]

The optical characteristics of doping superlattices (*n–i–p–i* doping schemes) are greatly improved by using the δ-doping technique. Quantum-confined optical transitions were observed in absorption[16] and photoluminescence experiments.[17] The improved doping superlattice structure, which has sawtooth-shaped band-edge potentials, allowed us to fabricate the first doping superlattice light-emitting diodes, current injection lasers, and tunable lasers.[18–20]

II. DEFINITION AND ELECTRONIC STRUCTURE OF δ-DOPED SEMICONDUCTORS

A one-dimensional doping profile in a semiconductor can be considered to be δ-function like, if the thickness of the doped layer is smaller as compared to other relevant length-scales. Specifically, it will be shown in this section that a doping distribution whose width is narrower than the electron de Broglie wavelength is δ-function like.

Assume a sheet of dopants, e.g., donors, in a semiconductor. Assume further a temperature range and density range which results in a complete ionization of the donors. In the picture of classical semiconductor physics, the free electron will migrate away from their parent ionized donors due to diffusion, i.e., random thermal motion of carriers. However, electrostatic attraction of electrons and donors is opposed to the diffusive motion and a balance of the drift and diffusive motion is achieved. The spatial extent of the electron gas (along the perpendicular direction to the donor plane) is given, in this classical picture, by the screening length such as the Debye length or the Thomas–Fermi length.

Even though the classical picture is qualitatively illuminating, it leads to quantitatively unsatisfactory results due to the neglect of size quantization. The size quantization of charge carriers becomes important if the potential energy (i.e., conduction band edge) changes significantly on the length scale comparable to the electron de Broglie wave-

length of thermal electrons (at $T = 300$ K electrons of kinetic energy $\frac{1}{2}kT$ correspond to a wave of length 300 Å in GaAs). A δ-function-like doping distribution is given by

$$N_D(z) = N_D^{2D}\delta(z - z_D), \tag{2}$$

where N_D^{2D} and z_D are the density and the location of dopants on the z axis, respectively. The charge distribution of Eq. (2) results in a potential energy of

$$E_C(z) = \begin{cases} -\dfrac{e^2 N_D^{2D}}{2\epsilon}(z - z_D) & \text{for } z \leqslant z_D \quad (3a) \\ +\dfrac{e^2 N_D^{2D}}{2\epsilon}(z - z_D) & \text{for } z \geqslant z_D \quad (3b) \end{cases}.$$

The potential well described by Eqs. (3a) and (3b) is V shaped and symmetric with respect to z_D. It can be easily verified that potential changes are indeed large on the length scale of the electron wavelength.

The conduction band diagram of a V-shaped potential well of δ-doped n-type GaAs is shown in Fig. 2 for a doping density of 5×10^{12} at $T = 4$ K. The electron distribution in the well is calculated by self-consistently solving Schrödinger's and Poisson's equation. Figure 2 reveals that four eigenstates are populated at the chosen doping density. The dopants are assumed to be 600 Å below the (unpinned) semiconductor surface and that the doping charge is distributed homogeneously over 2 Å. The calculation of the subband structure for different widths of the doping distribution (e.g., 0.2, 2, and 10 Å) reveals that the electronic structure is unaffected by the width of the doping distribution, as long as the spread of dopants is smaller than the spatial extent of the ground-state wave function. Insignificant changes in the electronic structure are found when the width of the dopant distribution is decreased to 1 or increased to 10 Å, i.e., much narrower than the spatial extent of the ($n = 0$) wave function, which has a spatial extent of ~ 50 Å. However, if the width of the doping distribution increases to values larger than the spatial extent of the ground state (e.g., 100 or 200 Å), changes of the electronic structure occur.

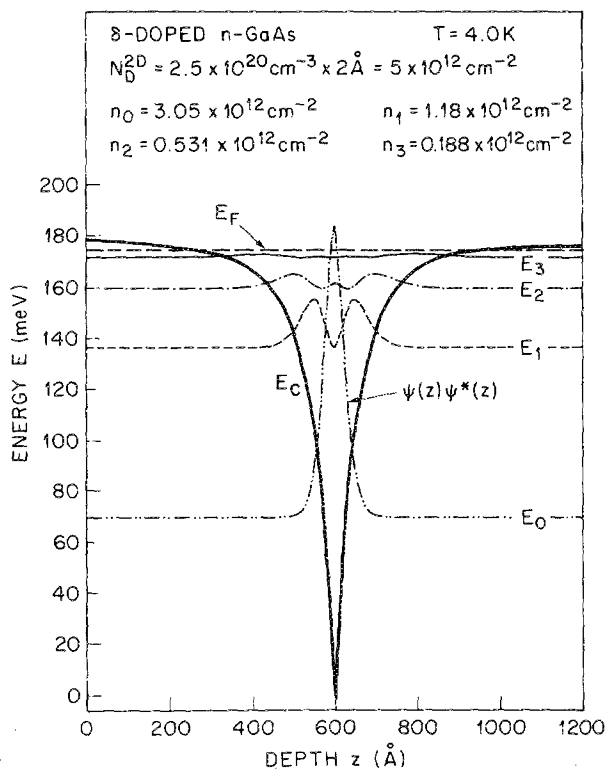

FIG. 2. Charge distribution in a δ-doped potential well obtained from the self-consistent solution of Poisson's and Schrödinger's equation. At a doping density of 5×10^{12} cm^{-2} four eigenstates are populated.

To quantify and generalize the requirement of spatial localization of dopants, the spatial extent of the ground state wave function is calculated using a variational approach.[17] The normalized trial function for the ground state is given by

$$\Psi_0(z) = \sqrt{2\alpha_0/5}(1 - \alpha_0 z)e^{+\alpha_0 z} \quad \text{for } z < 0, \tag{4a}$$

$$\Psi_0(z) = \sqrt{2\alpha_0/5}(1 + \alpha_0 z)e^{-\alpha_0 z} \quad \text{for } z \geqslant 0, \tag{4b}$$

where α_0 is the trial parameter. It is determined to be

$$\alpha_0 = \left(\frac{9}{4}\right)^{1/3}\left(e\mathbf{E}2m^*/\hbar^2\right)^{1/3}, \tag{5}$$

where $\mathbf{E}$ is the electric field of ionized dopants and is given by the derivative of Eq. (3), i.e., $\mathbf{E} = \pm eN_D^{2D}/2\epsilon$. The ground-state energy of the δ-doped structure is then given by

$$E_0 = \frac{3}{10}\left(\frac{9^2}{2}\right)^{1/3}\left(\frac{e^2\hbar^2\mathbf{E}^2}{2m^*}\right)^{1/3}. \tag{6}$$

The results for excited states will not be summarized here but can be found in the literature.[17]

Next, the spatial extent of the ground state is calculated. We define the spatial extent of the ground state as

$$z_0 = 2\sqrt{\langle z^2\rangle - \langle z\rangle_0^2}, \tag{7}$$

where $\langle z^2\rangle$ is the expectation value of the squared position and $\langle z\rangle_0$ is the position expectation value of the $n = 0$ state. If the definition of Eq. (7) is applied to a Gaussian wave function its spatial extent would be twice its standard deviation. Using the variational wave function used above, the spatial extent of the ground state wave function is determined to be

$$z_0 = 2\sqrt{\frac{7}{5}}\left(\frac{4}{9}\frac{\epsilon\hbar^2}{e^2N^{2D}m^*}\right)^{1/3}. \tag{8}$$

This equation easily allows us to determine z_0 for any host material or carrier type. For n-type GaAs with $N_D^{2D} = 5\times10^{12}$ cm^{-2} one obtains $z_0 = 46$ Å. This analytically calcuated extent is in agreement with the self-consistent numerical result shown in Fig. 2.

All dopant distributions of width much narrower than 46 Å can be considered as δ-function like for n-type GaAs at $N_D^{2D} = 5\times10^{12}$ cm^{-2}. Is not essential for the electronic subband structure of the semiconductor if dopants are confined to a monolayer of width < 1 Å, or if the width of the doping distribution is slightly wider, e.g., 10 Å. Both doping distributions (1 and 10 Å) can be considered as δ-function-like as long as their widths is $\ll 46$ Å.

The above consideration allows us to define a δ-doped semiconductor as a structure which contains a one-dimensional doping distribution confined to a narrow region,

whose thickness is small as compared to the ground-state wave function of the corresponding free carrier gas. Note that the spatial extent of the wave function [see Eq. (8)] depends on the doping density and the effective mass of the carrier. For example, heavier p-type carriers are more localized and thus require a narrower doping distribution in order to provide a δ-function-like doping profile.

In the next section it is experimentally shown that δ-function-like doping profiles can indeed be achieved. However, caution is required with some results reported in the literature. Not all claims of δ-doped semiconductors are approapriate. For example, doping distribution widths of 100 Å or more are definitely not δ-function-like.

III. SPATIAL LOCALIZATION OF DOPANTS

In this section, the spatial width of a dopant distribution is assessed by a structural probe and an electronic probe, namely secondary ion mass spectroscopy (SIMS) and the capacitance–voltage (C–V) profiling technique. Both techniques reveal that δ-function-like doping distributions are achieved for Si, Be, and C in GaAs and Si in $Al_xGa_{1-x}As$.

The δ-doped GaAs epitaxial layers are grown in a Varian Gen II molecular-beam epitaxy (MBE) system and a Vacuum Generator Gas-Source MBE system on semi-insulating, Zn-doped and Si-doped (001) GaAs substrates at growth temperatures ranging from 500 to 700 °C. The GaAs growth rate is 0.9 μm/h. The epitaxial layer sequence for Be δ-doped GaAs consists of 3000 Å Be-doped GaAs, 1000 Å undoped GaAs, the Be δ-doped layer, and a 1000-Å thick GaAs top layer. Capacitance–voltage (C–V) measurements are performed on 250 μm radius Ti/Au (500/1500 Å) Schottky contacts using a Hewlett–Packard Impedance/Gain-Phase Analyzer. Typical measurement frequency is 1 MHz. Secondary ion mass spectra (SIMS) are obtained from a Physical Electronics *Phi 6300* system. The primary ion acceleration potential used is 3 kV. The raster diameter is 750 μm with 70% gated secondary ion detection. The crater depth is measured with a *Dektak II* depth profiler.

The SIMS doping profile of a sample containing three δ-doped Be spikes at 500, 1000, and 1500 Å below the GaAs surface is shown in Fig. 3. The density of Be atoms in each layer is $N_{Be}^{2D} = 4\times 10^{12}$ cm^{-2}. The growth temperature was 500 °C. The SIMS profile reveals three clearly resolved peaks at the anticipated depths of 500, 1000, and 1500 Å. The SIMS profile exhibits a full width half-maximum of 37 Å for the shallowest of the doped layers, which is the narrowest SIMS doping profile reported to date. The full width at half-maximum increases to 40 and to 53 Å for the impurity layer buried at 1000 and 1500 Å, respectively. The SIMS profile clearly indicates the strong spatial localization of Be in δ-doped GaAs grown at low substrate temperatures.

The resolution of SIMS profiles is limited by (i) roughening of the sputtered crater and (ii) the *knock-on* effect. The roughening of the sputtered crater increases with sputtering time, which is illustrated by the increasing width of the SIMS peaks in Fig. 3. The second limitation of the SIMS resolution is given by the *knock-on* effect where sputtering primary ions transfer their momentum inelastically to Be dopants and causes Be atoms to be implanted deeper into the crystal. To minimize the *knock-on* effect, we use a low acceleration potential of 3kV in our measurements.

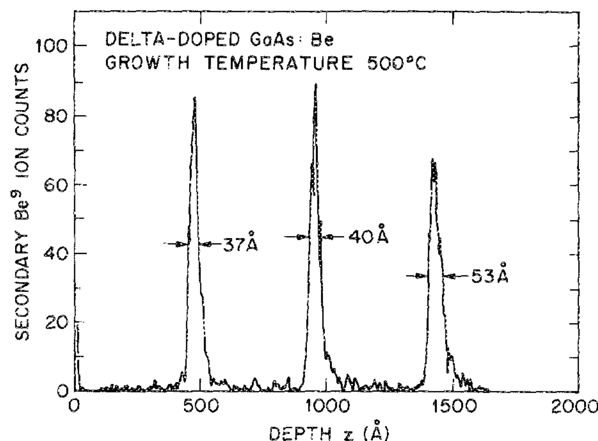

FIG. 3. Beryllium SIMS profile of a δ-doped GaAs sample with three doping spikes at 500, 1000, and 1500 Å below the epitaxial crystal surface.

Taking into account both intrinsic broadening mechanisms of the SIMS technique, we estimate the total broadening of the Be dopant profile to be less than three lattice constants ($\simeq$15 Å). Thus, δ-function-like doping profiles can be obtained in Be-doped GaAs.

Capacitance–voltage (C–V) profiles on a samples with a single δ-doped layer below the surface confirm the SIMS results. A (C–V) profile measured at room temperature on a sample grown at $T_s = 500$ °C is shown in Fig. 4. The profile has a full width at half-maximum of 20 Å and is the narrowest (C–V) profile reported in a semiconductor. The doping density can be determined from the sum of (i) free carriers

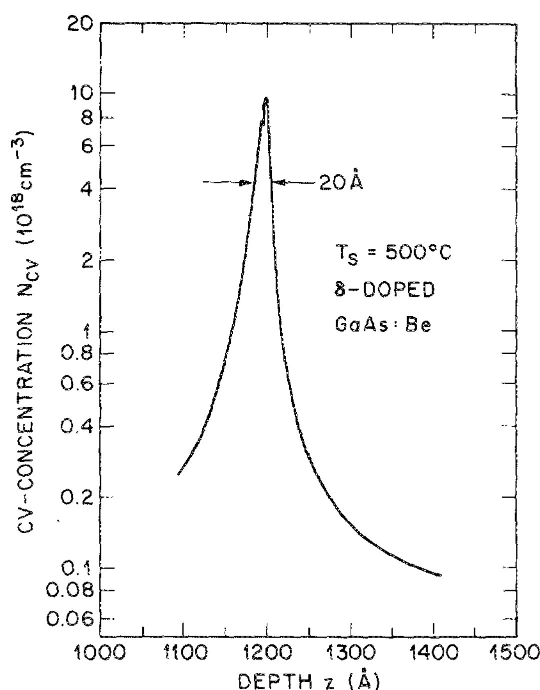

FIG. 4. Capacitance–voltage profile on a Be δ-doped GaAs sample ($N_A^{2D} = 4\times 10^{12}$ cm^{-2}) grown at 500 °C by molecular-beam epitaxy.

and (ii) carriers localized in surface states[5] assuming that all acceptors are ionized. The two-dimensional free carrier density can be determined from the integration of the profile. Following this procedure[5] one obtains $N_A^{2D} = 3.8 \times 10^{12}$ cm^{-2} for the profile illustrated in Fig. 4. The measured density is 5% lower than the doping density aimed for during crystal growth.

For a correct interpretation of the *C–V* profile it is important to recall that the *C–V* measurement is based on a free-carrier effect rather than a dopant effect. The spatial resolution of *C–V* measurements is limited by the classical Debye screening length and the Thomas–Fermi screening length for nondegenerately and degenerately doped semiconductors, respectively. However, the classical screening length limitation of the *C–V* technique is valid for classical semiconductors, i.e., without size quantization. In semiconductors with a size-quantized carrier system, the resolution of the *C–V* technique was recently shown to be given by the spatial extent of the wave function corresponding to the free carrier gas.[21] The authors[21] used second order perturbation theory to show that not the width of the doping distribution but rather the spatial extent of the (ground-state) wave function determines the resolution of the *C–V* technique. In δ-doped semiconductors the spatial extent of the ground-state wave function is given by [see Eq. (8)]

$$z_0 = 2\sqrt{\frac{7}{5}}\left(\frac{4}{9}\frac{\epsilon\hbar^2}{e^2 N^{2D} m^*}\right)^{1/3}, \tag{9}$$

as obtained from a variational wave function discussed above. The equation shows that even if the thickness of the doped layer approaches zero, the *C–V* profile width does not approach zero but rather the finite value given by Eq. (9).

Equation (9) allows us to estimate the *C–V* profile width for δ-doped GaAs using a doping density of $N_A^{2D} = 5 \times 10^{12}$ cm^{-2} and an effective mass of $m_{hh}^* = 0.45\ m_0$. One obtains $z_0 = 24$ Å in agreement with the experimental result shown in Fig. 4. It is concluded from the narrow *C–V* profiles on Be δ-doped GaAs that the total broadening of the true Be dopant profile is less than three lattice constants ($\cong 15$ Å). Both, the *C–V* technique and the SIMS technique thus yield a strong spatial localization of Be in δ-doped GaAs.

The spatial localization of dopants was also studied for Si *n*-type doped GaAs grown by gas-source MBE.[5] The study included a comparison of experimental and theoretical *C–V* profile widths at different Si doping densities. The Si densities employed range from 1.5 to 7.5×10^{12} cm^{-2}. The theoretical *C–V* profiles were obtained by a self-consistent quantum mechanical calculation, i.e., by simultaneously solving Schrödinger's and Poisson's equation. In the calculation, a top-hat distribution of $dz = 2$ Å and $dz = 50$ Å width were assumed.

The comparison of experimentally measured *C–V* profile widths (dark squares) and the calculated profile widths (two solid lines) are shown in Fig. 5. Furthermore, the approximate *C–V* profile width calculated analytically using the variational approach (for $dz \to 0$) as given by Eq. (9) is plotted in Fig. 5 as the dash-dotted curve. Inspection of Fig. 5 leads to the following conclusions: First, the experimental profile widths agree with calculated ones only if diffusion and other broadening mechanisms are irrelevant for the low growth temperatures employed in the study. Second, the variational calculation is in agreement with the quite elaborate self-consistent calculation in the entire doping density range. Delta-function-like doping profiles are thus feasible for Be and Si in GaAs.

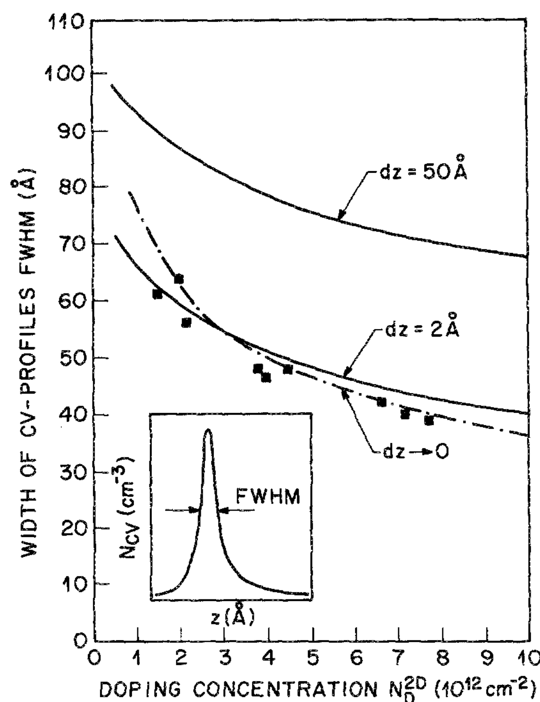

FIG. 5. Comparison of self-consistently calculated (—) and experimental (■) full widths at half-maximum of *C–V* profiles on δ-doped GaAs. Also included in the *C–V* profile width obtained from an analytic variational calculation (-·-) according to Eq. (9). Good agreement is obtained only if diffusion is assumed to be negligible.

The realization of δ-function-like doping profiles is limited to relatively low growth temperatures of $\leqslant 550$ °C. Epitaxial growth at temperatures exceeding 550 °C result in significant broadening of both, the SIMS and the *C–V* profiling technique. Certainly, the amount of doping spread at elevated growth temperatures depends on the species of impurity and host semiconductor. A quite pronounced *C–V* profile broadening was found for Si in $Al_xGa_{1-x}As$.[6]

The *C–V* profiles of growth-interrupted Si doping of $Al_{0.30}Ga_{0.70}As$ grown at 500, 600, and 700 °C is shown in Fig. 6.[6] At a growth temperature of 500 °C a profile width of 51 Å is measured. At elevated growth temperatures significant broadening to 118 and 305 Å occurs, which clearly illustrates the requirement of low growth temperatures for δ-doped $Al_xGa_{1-x}As$. The broadening of the doping distribution with elevated growth temperatures, as assessed by *C–V* and SIMS measurements, is observed for all impurities and host semiconductors.[5–9] However, the degree of broadening varies with the doping species and the host.

The physical origin of the doping profile broadening is an important question. Conventional impurity diffusion was identified as a major broadening mechanism.[22] In addition, preferential migration of impurities toward the growing surface was found for Si in GaAs.[23] Such a preferential migra-

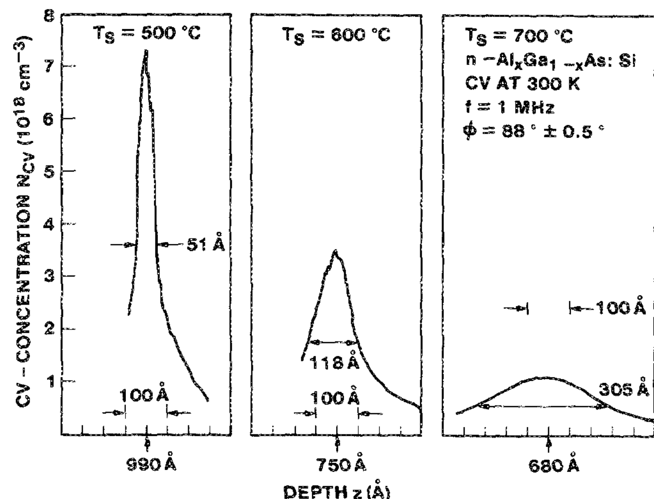

FIG. 6. Capacitance–voltage profiles of Si δ-doped $Al_xGa_{1-x}As$ grown at 500, 600, and 700 °C by molecular-beam epitaxy. Low substrate temperatures are required to spatially localize Si dopants in $Al_xGa_{1-x}As$.

tion of impurities cannot be explained by diffusion, since diffusion results in a symmetric broadening of the profile. In the next two sections, two broadening mechanisms, namely diffusion and Fermi-level pinning induced drift of impurities toward the surface will be investigated.

IV. DIFFUSION IN δ-DOPED SEMICONDUCTORS

Diffusion of impurities is a well known broadening mechanism for impurity distributions at elevated growth temperatures. However, the temperature dependence of the diffusion coefficients of Si and Be in GaAs and $Al_xGa_{1-x}As$ were unknown.[24] Recently, a sensitive method was developed,[22] which makes possible the determination of the temperature-dependent diffusion coefficient (600 °C ≤ T ≤ 1000 °C). The knowledge of the diffusion coefficients allows one to estimate the diffusion of impurities in δ-doped semiconductors during growth.

The novel technique to determine the diffusion coefficients of various impurities in III–V semiconductors employs the $C–V$ technique of rapidly thermally annealed δ-doped samples grown by MBE. The resolution of the technique is, if used appropriately, only few lattice constants and is more sensitive than other methods. The advantage of the method are especially in the low temperature domain (600 °C) and in the high temperature domain (1000 °C). At low temperatures little diffusion occurs, so that a sensitive technique is required. In the high temperature regime short diffusion times (e.g., 5 s) are required due to the lack of thermal stability of many compound semiconductors.

The epitaxial films used for the diffusion study are grown on n^+ or p^+-type (001) GaAs by MBE at 500 to 550 °C. The layer sequence consists of a doped buffer layer, a 1000-Å thick undoped layer, the δ-doped, layer and a 1000–1500-Å thick cap layer. The density of the δ-doped layer is 4–6 × 10^{12} cm^{-2}. The wafer is cleaved into several pieces, which are annealed at temperatures ranging from 600 to 1000 °C for 5 s. Samples containing impurities with low diffusivity (e.g., carbon) may require longer annealing times, especially at low annealing temperatures to provide a measurable diffusion length. An AG-Associates Heatpulse AG-410 rapid thermal annealing furnace is used for the temperature cycle. A AuGe/Ni/Au (2000/1500/2000 Å) metallization alloyed at 420 °C for 30 s is used for ohmic backside contacts. Circular Ti/Au (500/1500 Å) Schottky contacts with a diameter of 500 μm are evaporated through a shadow mask. The $C–V$ characteristics are measured on a Hewlett-Packard 4194A Impedance Gain-Phase analyzer. The current-voltage phase angle is 88° ± 1° at a frequency of 1 MHz, indicating the dominating capacitive character of the Schottky contacts. $C–V$ concentration versus depth profiles were obtained from $C–V$ curves using well-known equations. Additional current–voltage characteristics yielded a good ideality factor of $n = 1.04$.

The $C–V$ profiles of six pieces of a Be δ-doped GaAs sample annealed at different temperatures is shown in Fig. 7. The figure reveals a systematic broadening of the profile from 34 to 440 Å for the pieces annealed at 600 and 1000 °C, respectively. (The profile of the unannealed sample is shown in Fig. 4 and has a width of 20 Å.) Furthermore, the peak concentration of the $C–V$ profiles drops from ≅ 10^{19} cm^{-3} to ≅ 10^{18} cm^{-3}.

The integration of the $C–V$ profiles yields the free carrier density, that is

$$p_{2DHG} = \int_z N_{CV} dz, \quad (10)$$

where p_{2DHG} is the two-dimensional hole density. The density p_{2DHG} remains constant for all annealing temperatures, which indicates that Be occupies substitutional cation sites before and after the annealing process. The $C–V$ density and the Be density obtained from SIMS measurements coincides within ± 10%, which indicates that all Be impurities are

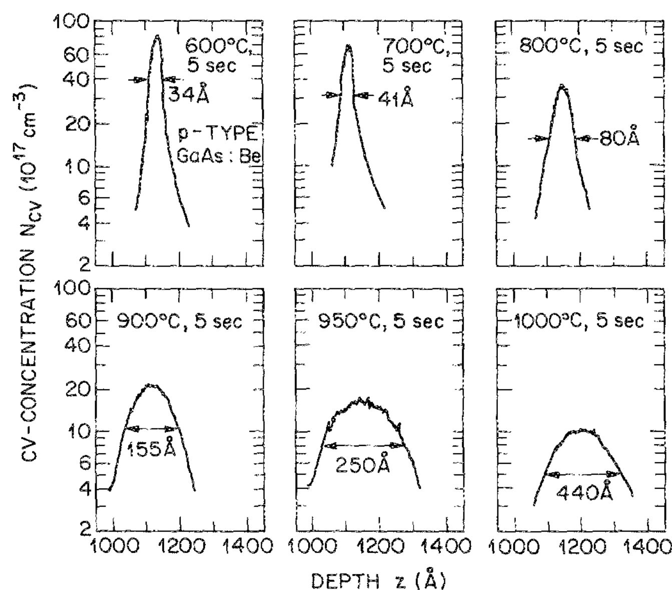

FIG. 7. Capacitance–voltage profiles of different pieces of a Be δ-doped GaAs sample rapidly thermally annealed at temperatures 600 °C ≤ T ≤ 1000 °C for 5 s.

electrically active. Therefore, the broadening of the C–V profiles is representative for the broadening of the Be doping profile.

The theoretical analysis of diffusion of Si impurities in δ-doped GaAs samples is straightforward. We assume an initial distribution according to the Dirac-delta function

$$N_A(z) = N_A^{2D}\delta(z - z_0), \quad (11)$$

and obtain a Gaussian distribution with diffusion length $L_D = \sqrt{D\tau}$ after diffusion:

$$N_A(z) = N_A^{2D}(4\pi D\tau)^{-1/2}\exp\left(-\frac{(z-z_0)^2}{4D\tau}\right). \quad (12)$$

This normal distribution represents a solution of the one-dimensional Fickian diffusion equation. The diffusion time is denoted at τ and D is the so-called diffusion coefficient, which depends on temperature according to

$$D = D_0 \exp(-E_a/kT), \quad (13)$$

where E_a is the activation energy of the diffusion process, k is Boltzmann's constant, and T the absolute temperature.

The extraction of the diffusion length from the experimental data shown in Fig. 7 can be performed by (i) a comparison of experimental C–V profiles with self-consistently calculated ones[22] or (ii) by using analytic approximations.[6,22] In the analytic approximation it is assumed that the broadening of the C–V profile is due to an intrinsic term σ_i and a diffusion-induced term σ_{diff} such that the total broadening of the C–V profile is given by

$$\sigma^2 = \sigma_{\text{diff}}^2 + \sigma_i^2. \quad (14)$$

(Strictly speaking, the validity of this equation is limited to Gaussian functions.) In the absence of diffusion processes, the width of the C–V profile ($\cong 2\sigma$) is determined by the intrinsic resolution of the C–V technique, i.e., $2\sigma_i = z_0$. For large diffusion lengths the width of the C–V profile (2σ) is determined by the diffusion broadening ($2\sigma_{\text{diff}}$). Note that the diffusion length and the standard deviation σ of the Gaussian function are related by

$$\sigma = \sqrt{2}L_D = \sqrt{2D\tau}. \quad (15)$$

Thus, the diffusion coefficient D can be determined for each annealing temperature using Eqs. (11)–(15).

Using the above described technique, the diffusion coefficients of several impurities were determined including Si in GaAs,[22] Si in $Al_xGa_{1-x}As$,[6] Be in GaAs,[7] and C in GaAs.[21] The diffusion coefficients of Si, Be, and C in GaAs are shown in Fig. 8 as a function of temperature. At a temperature of 500 °C the diffusion coefficients are below 10^{-17} cm^2/s indicating that little diffusion (< 10 Å) occurs for typical δ-doped samples. Thus, the diffusion coefficients of impurities in GaAs are sufficiently small to make possible the growth of δ-doped semiconductors.

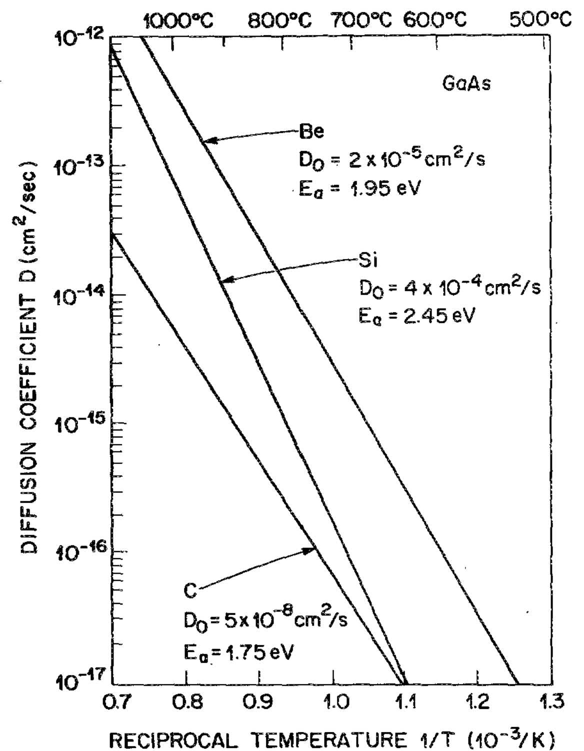

FIG. 8. Diffusion coefficient of, C, and Si, Be in GaAs vs reciprocal temperature.

V. FERMI-LEVEL PINNING INDUCED SEGREGATION

The study of the broadening of δ-function-like doping distributions revealed a preferential migration of impurities toward the semiconductor surface during epitaxial growth.[8,23,25,26] The preferential surface migration cannot be explained by simple diffusion, since diffusion results in a symmetric (Gaussian-type) broadening. To explain the surface migration, classical surface segregation,[23] solubility-limit segregation,[8] and Fermi-level-pinning induced segregation were proposed.[26] In the following experimentally obtained asymmetric impurity redistribution is illustrated for Si in $Al_xGa_{1-x}As$ and the model of Fermi-level-pinning induced segregation is presented.

$Al_xGa_{1-x}As$ and GaAs epitaxial layers are grown in a Varian Gen II system at 500, 580, and 660 °C. The buffer layer is followed by 1000 Å of $Al_xGa_{1-x}As$, a delta-function-like doping profile of Si with $N_{\text{Si}}^{2D} = 2$–4×10^{12} cm^{-2} and a final 1000-Å thick $Al_xGa_{1-x}As$ layer. Secondary ion mass spectroscopy (SIMS) measurements are carried out on a PHI 6000 and an Atomica instrument with Cs^+ and O_2^+ ion sputtering and an acceleration potential of 3 kV.

Si-dopant profiles obtained from SIMS are shown in Fig. 9 for the three samples grown at 500, 580, and 660 °C. At a low growth temperature a sharp peak is observed in agreement with earlier results. The slight asymmetric shape of the SIMS profile obtained at low growth temperature is due to the well-known *knock-on* effect. As the growth temperature is increased the profiles exhibit significant asymmetry. Surface segregation of dopants is evident from the profiles, especially at $T_s = 660$ °C. The steepness of the leading and the trailing slope of the SIMS spectrum are evaluated in terms of the length in which the Si signal decreases by one order of magnitude. The leading slope increases from 35 to 390 Å/decade indicating the *surface migration* of dopants. The trailing slope increases from 80 to 140 Å/decade and indicates diffusion of dopants, which is expected to be symmetric with respect to both sides of the structure. We observe qual-

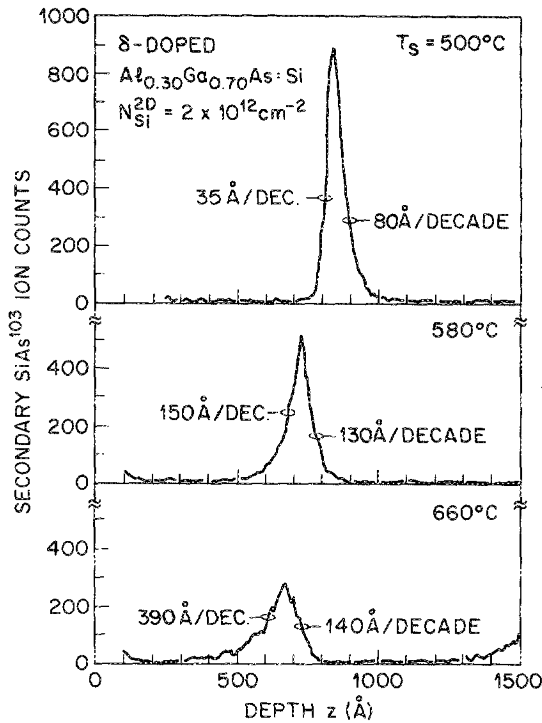

FIG. 9. Secondary ion mass spectroscopy profiles of Si δ-doped $Al_xGa_{1-x}As$ grown at 500, 580, and 660 °C by molecular-beam epitaxy. At elevated substrate temperatures, segregation, i.e., migration of dopants predominantly along the growth direction, is observed.

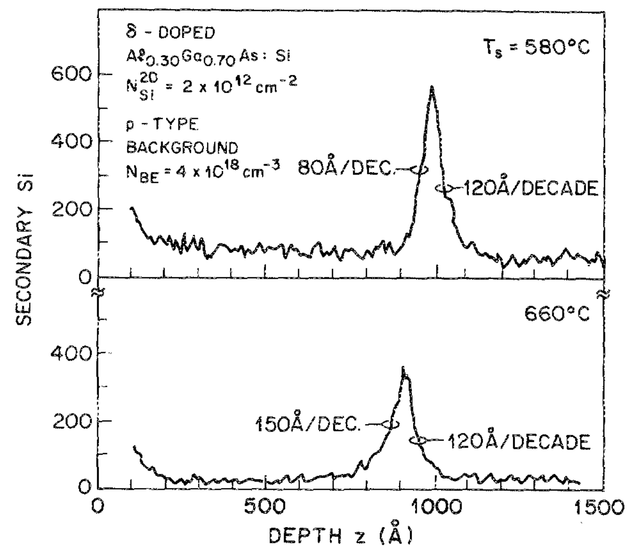

FIG. 10. Secondary ion mass spectroscopy profiles of Si δ-doped $Al_xGa_{1-x}As$ grown at 580 and 660 °C, which contains intentional p-type background doping. A reduction of segregation is observed upon p-type background doping.

itatively the same but quantitatively weaker surface segregation for Si in GaAs. For the sake of clarity we show only the data obtained on Si-doped $Al_xGa_{1-x}As$.

Fermi-level pinning at the semiconductor surface causes the doped layer to be depleted of the free carriers and a localization of electrons in surface states. If the resulting dipole field is the driving force towards surface segregation, then this segregation process can be reduced by screening the dipole field. Figure 10 shows two SIMS profiles in which a p-type Be background doping is included. The concentration of Be is chosen to be $N_A = 4 \times 10^{18}$ cm^{-3} in order to compensate for the Si dopants within 50 Å. Figure 10 reveals that the segregation length is drastically reduced from 150 to 80 Å/decade at a growth temperature of 580 °C. The decrease of the segregation length is attributed to the screening of the surface dipole caused by Fermi-level pinning. The trailing slope of the SIMS profile is changed insignificantly indicating that diffusion *knock-on* effect are not influenced by background doping. The SIMS profile for the sample grown at $T = 660$ °C shows the same qualitative trend as the sample grown at the intermediate temperature (see Figs. 9 and 10). The surface segregation length is reduced and the SIMS profile has a more symmetric shape, indicating that diffusion dominates the dopant redistribution. The results show that the (electronic) property of Fermi-level pinning causes significant redistribution of dopants during growth and that this interaction can be screened by appropriate background doping.

Traditional theories of surface segregation are based on the concept that a lower (structural) surface energy and a higher volatility of impurities are the driving forces toward surface segregation. Hitherto Fermi-level pinning was not identified as a driving force towards segregation.

Fermi-level pinning at an interface of a semiconductor and a second medium, such as a metal, insulator, or vacuum is a classic phenomenon in semiconductor physics. The Fermi level at the interface is pinned at an energy $e\phi_B$ below the bottom of the conduction band. Bardeen attributed Fermi-level pinning to interface states which are of donor and acceptor type. Energetically such Bardeen states can be in the conduction or valence band (e.g., for InAs); more frequently the states are located close to the middle of the fundamental gap (e.g., GaAs). Fermi-level pinning occurs in a wide range of temperatures and the pinning energy is approximately independent of temperature.[27] This is consistent with the fact that the thermal energy kT is much smaller than other relevant energies. Direct gap $Al_xGa_{1-x}As$ ($x < 0.37$) is known to have a very similar band structure as GaAs.[10] Furthermore, properties related to Fermi-level pinning, such as Schottky-barrier height and surface depletion, are known to be very similar for GaAs and direct-gap $Al_xGa_{1-x}As$.[10] Therefore, even though less data is available for $Al_xGa_{1-x}As$, we assume that the Fermi level is pinned during crystal growth of GaAs and $Al_xGa_{1-x}As$ and we will focus on the consequences of such pinning.

To date, the well-known physical *consequences* of Fermi-level pinning are (i) the rectifying characteristics of metal–semiconductor contacts and (ii) the depletion of semiconductor surfaces from free carriers. In the following a further consequence of Fermi-level pinning, i.e., the modification of doping distributions during crystal growth, is analyzed.

The band diagram of a semiconductor containing a δ-function-like doping profile is shown in Fig. 11(a). Figure 11(b) shows that inclusion of appropriate background doping results in *reversal of the surface electric field*, which represents a driving force for impurities toward the substrate.

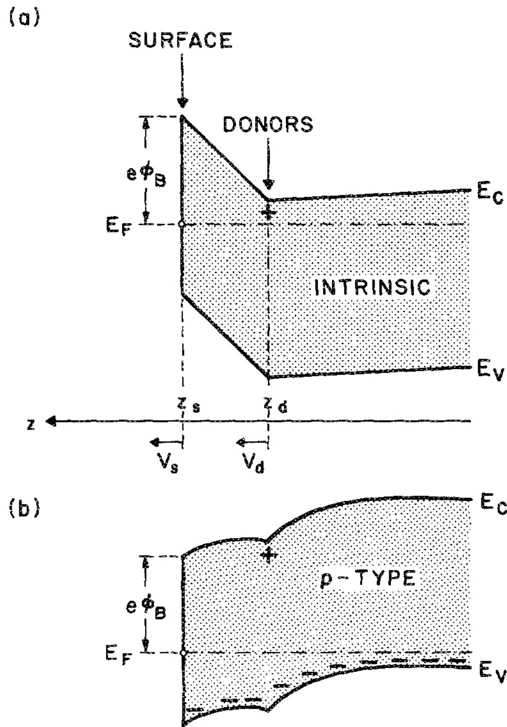

FIG. 11. Band diagram of a (a) growing n-type δ-doped semiconductor. The surface moves at a velocity v_s. Dopants segregate at a velocity v_d. (b) Inclusion of p-type background doping reverses the electric field at the semiconductor surface.

The surface of the semiconductor is assumed to be moving along the z direction with a velocity v_s. For a two-dimensional doping density of N_D^{2D} the electric field of the dipole is given by

$$\mathbf{E} = eN_D^{2D}/\epsilon, \tag{16a}$$

$$\mathbf{E} = \phi_B/(z_s - z_d), \tag{16b}$$

where e is the elementary charge, ϵ is the permittivity, and $z_s = v_s t$ and z_d are the position of the surface and the doped layer, respectively, Equation (16a) is valid if the doped layer is depleted of all free carriers, i.e., $z_s - z_d \ll \phi_B \epsilon / eN_D^{2D}$, while Eq. (16b) is valid if the doped layer is partly depleted of free carriers, i.e., $z_s - z_d \gg \phi_B \epsilon / eN_D^{2D}$. The segregation velocity of dopants is given by

$$v_d = \frac{dz_d}{dt} = \mu \mathbf{E}, \tag{17}$$

where μ is the doping ion mobility which is obtained from the diffusion coefficient of Si in $Al_xGa_{1-x}As$[6] ($D_0 = 4 \times 10^{-8}$ cm^2/s, $E_a = 1.3$ eV) and the Einstein relation $\mu = De/kT$.

For small distances between the doped layer and the surface, the dipole field is given by Eq. (16a) and the segregation velocity of the dopants is given by

$$v_d = \frac{De}{kT} \frac{eN_D^{2D}}{\epsilon}. \tag{18}$$

At 500 °C the diffusion coefficient is $D = 2.5 \times 10^{-16}$ cm^2/s and Eq. (4) yields $v_d = 0.1$ Å/s for the segregation velocity which is a small velocity. However, at $T = 660$ °C one obtains $D = 6 \times 10^{-15}$ cm^2/s where the segregation velocity is 2 Å/s, which is comparable in magnitude to the growth velocity (v_g) of 1.29 μm/h = 3.6 Å/s for $Al_{0.30}Ga_{0.70}As$ (0.9 μm/h for GaAs). Thus, significant segregation is expected to occur at $T = 660$ °C.

To obtain a single differential equation for small $(z_s - z_d)$ and large $(z_s - z_d)$ the electric field given in Eqs. (16a) and (16b) is approximated by

$$\mathbf{E} = \left[\left(\frac{e}{\epsilon} N_D^{2D}\right)^{-1} + \left(\frac{\phi_B}{z_s - z_d}\right)^{-1}\right]^{-1}, \tag{19}$$

which represents a lower limit of the true field in the intermediate range. The differential equation then becomes

$$\frac{dz_d}{dt} = \frac{De}{kT}\left(\frac{\epsilon}{eN_D^{2D}} + \frac{z_s - z_d}{\phi_B}\right)^{-1}, \tag{20}$$

with $z_s = v_s t$. We solved this nonlinear differential equation numerically for the three growth temperatures, a (experimental) carrier density of $N_D^{2D} = 2 \times 10^{12}$ cm^{-2}, and a total growth time of $t = 280$ s. The results of the numerical solution are as follows: At low substrate temperature of 500 °C the segregation during growth of the 1000-Å thick top layer is 12 Å. The corresponding calculated segregation length at the growth temperatures of 580 and 660 °C are 64 and 293 Å, respectively. These calculated segregation lengths are in good qualitative agreement with the experimental results displayed in Fig. 9.

These approximate calculations allow us to estimate the relative importance of the diffusion and the segregation process. The diffusion length is known to equal approximately $\sqrt{Dt}$. According to Eq. (20), the segregation length is proportional to Dt. Since D depends exponentially on temperature, diffusion ($\sqrt{Dt}$) dominates at low temperatures, while segragation (Dt) will dominate at higher temperatures; this trend is clearly confirmed by our experiments.

The calculation above, although it gives a very good explanation of the physical process causing surface segregation, is unrealistic in two respects. First, since diffusion of impurities was neglected, the impurity profile remains δ-function like. The second insufficiency of the calculation is the omission of screening. At the growth temperature of 660 °C the concentration of thermally excited, intrinsic carriers reaches a value of $n_i \cong 10^{16}$ cm^{-3} which corresponds to a Debye screening length of $\cong 550$ Å.

The understanding of the segregation mechanism opens up new ways to either make use of the mechanism or to avoid segregation in these semiconductors. The possible uses include the controlled field-driven redistribution of dopants close to the surface. On the other hand, possibilities to reduce the segregation include (i) illumination of the growing surface to increase the carrier density and the screening, (ii) growth on different surface orientations such as the (110) plane on which the Fermi-level pinning is possibly absent, and (iii) growth at low temperatures.

VI. DELTA-DOPED FIELD EFFECT TRANSISTORS

The δ-doping technique represents the ultimate limit for scaling of doping profiles. Such scaling of the dimensions of a semiconductor structure is of importance for semiconductor devices. As the spatial lateral and vertical dimensions of devices shrink, the switching speed and the power consumption of the device decrease. It is thus of fundamental interest to investigate field effect transistors with doping profiles scaled to their ultimate limit.

A field effect transistor which contains a δ-function-like doping profile is shown in Fig. 12. The doped layer is sandwiched between nominally undoped GaAs, which is epitaxially grown on GaAs. The δ-doped field effect transistor (FET)[10,28] shown in Fig. 12 has a number of advantages over conventional, homogeneously doped MESFETs, including (i) short gate-to-channel distance, (ii) high transconductance, (iii) high densities of the 2DEG, (iv) large breakdown voltage, and (v) reduced short channel effects. The intrinsic transconductance of a FET can be given in analytic form according to

$$g_m^* = \frac{1}{L_G} (e\mu W_g n_{2\mathrm{DEG}}) \left[1 + \left(\frac{e\mu n_{2\mathrm{DEG}} d}{e v_s L_G} \right)^2 \right]^{-1/2}, \tag{21a}$$

where W_G, L_G, and d are the width and the length of the gate, and the distance between the gate and the 2DEG, respectively. The saturation velocity is designated as v_s. For short gate lengths $L_G \to 0$ the equation reduces to

$$g_m^* = \epsilon v_s W_G / d, \tag{21b}$$

which can also be derived from the well-known saturation-velocity model. Equation (21a) is based on a two-region model for the velocity-field characteristic and a velocity saturation at the drain end of the gate.[20,30] The equation suggests that a short gate-to-channel d is desirable and yields a high transconductance. An intrinsic transconductance exceeding 500 mS/mm was estimated for the δ-doped FET.[28]

A high carrier density of the 2DEG is desirable as well to achieve a high transconductance, as concluded from Eq. (21). Since high carrier densities are easily achievable by the δ-doping technique, a high transconductance is feasible. Note that the densities of the 2DEG can exceed the densities achievable in selectively doped heterostructure transistors.

A further advantage of the δ-doped FET is the large gate breakdown voltage. The maximum electric field under the gate is *smaller* for the δ-doped FET as compared to the conventional, homogeneously doped FET.[28] A large breakdown voltage is consequently observed in δ-FETs.

Finally, short-channel effects are less pronounced in δ-doped FETs. Short channel effects are prominent if the gate length becomes smaller than the gate-to-channel distance, short channel effects manifest themselves as a lack of pinch off, large output conductance, etc. Thus, the δ-doped FET with its inherently small gate-to-channel distance has advantageous properties in the short gate-length domain. Little short-channel effects are expected for the δ-doped FET for gate lengths as small as 1000 Å. The output current–voltage characteristic of a depletion-mode δ-doped FET is shown in Fig. 13. The field effect transistor is fabricated in a two-mask self-aligned process.[31] The transconductance of the transistor is 240 mS/mm at a gate length of $L_g = 1.3\ \mu$m. The output characteristic exhibits excellent pinch off, current saturation, and turn-on resistance. In addition to depletion mode transistors, also enhancement mode transistors were fabricated.[31] More recently, δ-doped transistors with a transconductance of 270 mS/mm were fabricated.[32]

Selectively doped heterostructure transistors (SDHTs) take advantage of (i) the enhanced electron mobility in such heterostructures and (ii) the spatially well-defined two-di-

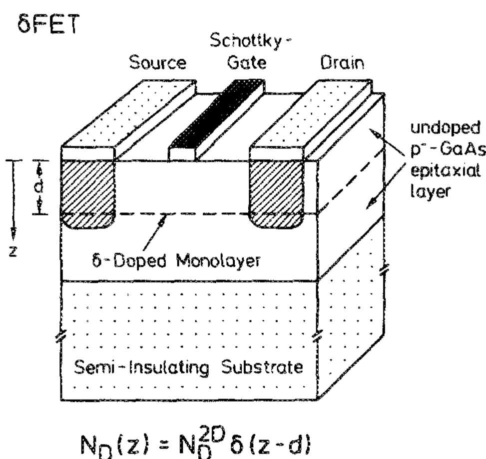

FIG. 12. Delta-doped GaAs metal–semiconductor field effect transistor. The conductive channel in a Si δ-doped layer located at a distance d below the Schottky gate.

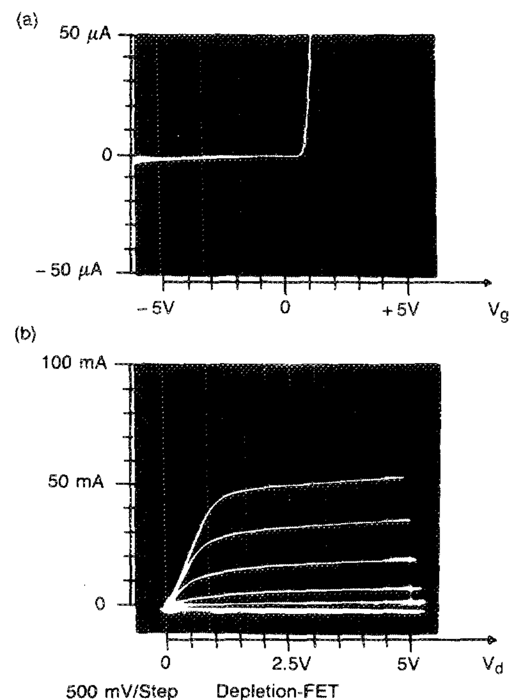

FIG. 13. (a) Gate-source and (b) drain-source current–voltage characteristics of a δ-doped depletion-mode MESFET with a gate length of 1.3 μm and a width of 150 μm. A peak transconductance of 240 mS/mm is measured on the device. The gate voltage is + 0.5 V for the top drain current trace.

mensional electron gas (2DEG). An extensive review on SDHTs was given by Pei and Shah.[33] Today, SDHTs, also called high electron mobility transistors (HEMTs), two-dimensional electron-gas field-effect transistors (TEGFETs) or heterostructure field-effect transistors (HFETs) are used in high-speed integrated circuits and for low-noise microwave applications.

An important figure of merit of SDHTs is the density of the 2DEG at the heterointerface.The density is determined by the inherent properties of the heterostructure, such as the conduction band discontinuity, the spacer thickness, and the doping concentration. Densities are typically limited to $\lesssim 1\times 10^{12}$ cm^{-2} in the $Al_xGa_{1-x}As$ system. However, higher densities are desirable to improve the transconductance of the transistor.

Employment of the δ-doping technique allows one to enhance the density in selectively doped heterostructures over values achievable in conventional, homogeneously doped SDHTs.

The energy-band diagrams of the selectively δ-doped heterostructure (SΔDH) and the conventional selectively doped heterostructure (SDH) are shown in Figs. 14(a) and 14(b), respectively. In the SΔDH, all donor impurities are localized in a plane at a distance W_s from the

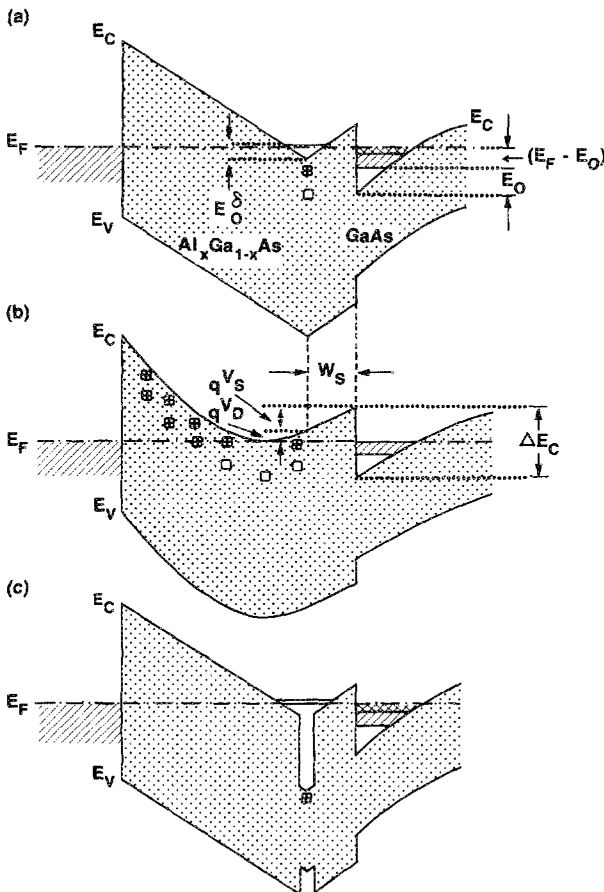

FIG. 14. Schematic energy-band diagram of a (a) selectively δ-doped heterostructure and a (b) homogeneously doped heterostructure. A heterostructure (c) which is δ-doped in a GaAs quantum well avoids persistent photoconductivity effects.

$Al_xGa_{1-x}As$/GaAs interface. The donor localization results in a V-shaped quantum well with a lowest subband energy of E_0^δ. In the conventional SDH, the $Al_xGa_{1-x}As$ conduction band has a parabolic shape [Fig. 14(b)] with negligible size quantization. For the *selectively δ-doped heterostructures* we can write the energy balance:

$$\Sigma E = 0 = -E_0 - (E_F - E_0) + \Delta E_c - e\mathbf{E}W_s + E_0^\delta + (E_F - E_0^\delta), \quad (22a)$$

where E_0 is the lowest subband energy of the 2DEG, $(E_F - E_0)$ is its degeneracy, ΔE_c is the conduction-band discontinuity, and **E** is the electric field within the spacer. The energy E_0^δ is the ground state energy in the V-shaped potential well of the δ-doped $Al_xGa_{1-x}As$. The term $(E_F - E_0^\delta)$ can be assumed to be zero, i.e., there are no mobile carriers in the $Al_xGa_{1-x}As$. In Eq. (22a) we assume that none of the two quantum wells (V-shaped quantum well in the $Al_xGa_{1-x}As$, and triangular well at the semiconductor interface) perturbs the eigenstate energy of the other corresponding quantum well. For the *homogeneously selectively doped* heterostructure (SDH) we can write the following sum of energies:

$$\Sigma E = 0 = -E_0 - (E_F - E_0) + \Delta E_c - e\mathbf{E}W_s - eV_D, \quad (22b)$$

where V_D is the potential drop within the depletion region, as shown in Fig. 14(b). Comparison of Eqs. (22a) and (22b) yields two differences. First, in the SΔDH, the eigenstate energy in the V-shaped quantum well of the $Al_xGa_{1-x}As$, E_0^δ, adds up to the barrier height, ΔE_c. Therefore, we can understand the sum $(E_0^\delta + \Delta E_c)$ as an "*effective conduction-band discontinuity*" which is *enhanced* as compared to the conventional SDH. Second, the potential drop in the depletion region [Eq. (22b)], $-qV_d$, does *not* enter Eq. (22a). The depletion width approaches zero thickness due to the *localization of donor impurities* in the δ-doped $Al_xGa_{1-x}As$. The SΔDH has consequently two advantages: (i) effective discontinuity enhancement due to size quantization in the $Al_xGa_{1-x}As$ and (ii) absence of depletion-region potential drop due to localization of donor impurities in the δ-doped $Al_xGa_{1-x}As$. Both characteristics will result in the desired increase of the density of the 2DEG. The increase in concentration was previously calculated in greater detail.[11,34,35]

An interesting structure is shown in Fig. 14(c), which uses a GaAs quantum well which is δ doped. If the GaAs quantum well is thin enough (<10 Å), the eigenstate energy in the $Al_xGa_{1-x}As$ is not purturbed significantly. Such a structure would maintain the advantages of the SΔDH and, in addition, would reduce the problem of persistent photoconductivity associated with the deep donor in the $Al_xGa_{1-x}As$ by spatially separating donors from the $Al_xGa_{1-x}As$.

A high density 2DEG is indeed observed in the selectively δ-doped heterostructures. The magnetoresistance of a SΔDH is shown in Fig. 15(a). Shubnikov–de Haas oscillations with two distinct periods are observed and indicate the first observation of two subbands being occupied in an $Al_xGa_{1-x}As$/GaAs heterostructure. We attribute the two

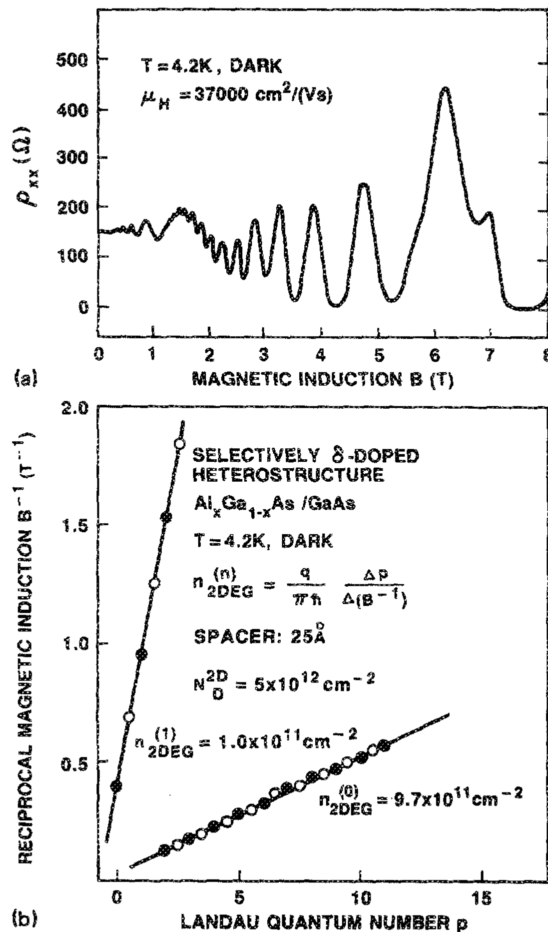

FIG. 15. (a) Low-temperature magneto resistance of a selectively δ-doped heterostructure. (b) Evaluation of the two periods of the Shubnikov–de Haas oscillations yields a density of 9.7×10^{11} cm^{-2} and 1.0×10^{11} cm^{-2} at low temperature for the lowest and the first excited subbands, respectively.

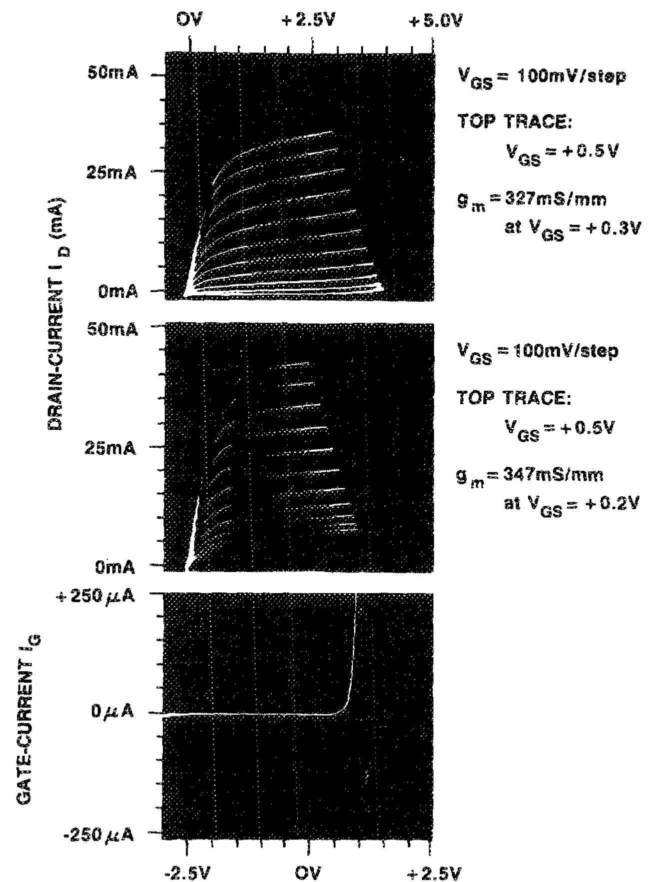

FIG. 16. Drain current vs drain source voltage of a selectively δ-doped heterostructure transistor with a transconductance of up to 347 mS/mm. A gate-source current–voltage characteristic is shown in the lower part.

oscillations to the lowest and first excited subbands of the 2DEG. The density within the two subbands are evaluated by plotting the Landau quantum numbers of the minima (solid circles) and maxima (open circles) versus reciprocal magnetic induction, as shown in Fig. 15(b). The slope of this plot yields the densities of 9.7×10^{11} cm^{-2} and 1×10^{11} cm^{-2} for the lowest and first excited subbands, respectively. The total density is $n_{2DEG} = 1.07\times10^{12}$ cm^2 at 300 mK. The corresponding mobility is $\mu = 37\,000$ cm^2/V s. At room temperature a density of $n_{2DEG} = 1.7\times10^{12}$ cm^{-2} and a mobility of 8900 cm^2/V s have been obtained from Hall measurements on the same sample.

Conventional selectively doped heterostructure transistors have typical densities of $n_{2DEG} < 1\times10^{12}$ cm^{-2}. The high 2DEG density that can be obtained in the selectively δ-doped heterstructures is favorable for field effect transistor performance. In Fig. 16 we show the output characteristics of two *depletion-mode* SΔDHTs. The SΔDHTs have low ON resistance ($R_{ON} = 1.83$ Ω mm), excellent saturation characteristics, low differential output conductance in the saturation regime, and good pinch-off characteristics. A very high transconductance of up to $g_m = 360$ mS/mm is obtained from the SΔDHT. Transconductances of 320–360 mS/mm are measured in a considerable number of SΔDHTs on the same wafer. The processed wafers have good homogeneity and yield. The contact resistance is measured to be $R_c = 0.07$ Ω mm. At a low temperature of $T = 77$ K a transconductance of $g_m = 420$ mS/mm is obtained. The lower part of Fig. 16 shows the gate-source current–voltage characteristic. A large breakdown voltage of $V = -6$ V is measured in the reverse direction.

VII. DELTA-DOPED DOPING SUPERLATTICES

Doping superlattices consist of semiconductors, which are alternatingly doped with n-type and p-type impurities. The period of such doping superlattices is typically 100 to 2000 Å. Due to the proximity of the n-type and the p-type layers, electrons recombine with holes. If the doping superlattices contain an equal density of donor and acceptor impurities then the superlattice is depleted of free carriers. A periodic potential results from the ionized impurity changes. The periodic superlattice potential has several far-reaching consequences which will be discussed in the following.

The doping profile of a doping superlattice containing alternating n-type and p-type δ function is shown in Fig. 17. The superlattice has a period of z_p and the doping spikes (which are separated by $z_p/2$) have a two-dimensional density of N_D^{2D} and N_A^{2D} for donors and acceptors, respectively. The sawtooth-shaped band diagram resulting from the δ-

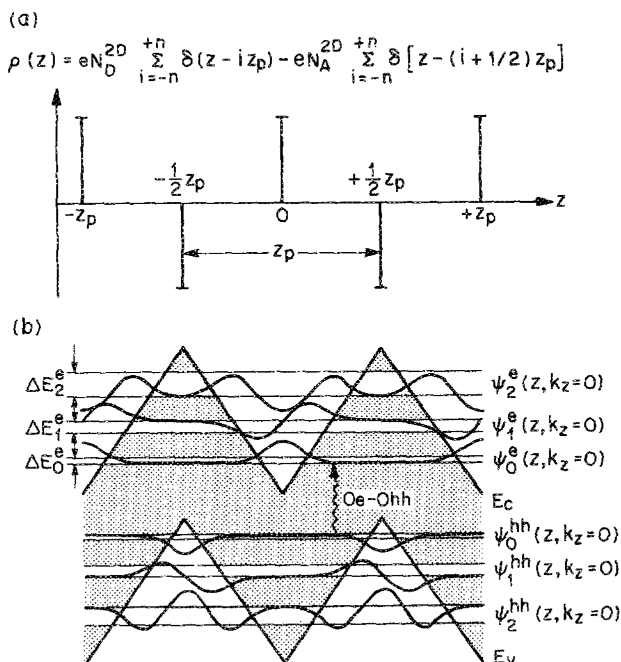

FIG. 17. (a) Doping profile of a δ-doped doping superlattice consisting of a train of alternating n-type and p-type δ functions. (b) Schematic band diagram and wave functions of the sawtooth doping superlattice. The wave functions $\Psi_n(z)$ are shown for $k_z = 0$. Minibands have a width of ΔE_n.

function-like doping profile is shown in the lower part of Fig. 17. Also sketched are the three lowest subband or miniband states of the doping superlattice. Note that the position expectation values of electron and hole wave functions are displaced by half a superlattice period, i.e., electrons and holes are spatially separated.

The band diagram illustrates some interesting features of doping superlattices. First, the superlattice energy gap, i.e., the transition energy between the lowest conduction subband and the highest valence subband, is smaller than the gap energy of the host semiconductor. As an example the absorption transition 0e–0hh (ground-state heavy hole to ground-state electron) illustrated in Fig. 17 is clearly smaller than the gap energy of the host semiconductor. Second, electron and hole wave function are spatially displaced by half a superlattice period, $z_p/2$. Consequently, the overlap integral between the states and the oscillator strength of the transitions can be smaller, as compared to a bulk semiconductor. The lifetime of radiative transitions can be enhanced especially for long periods ($\gg 100$ Å) of the doping superlattice. Third, doping superlattices of sufficiently long periods exhibit *tunability* of their effective gap energy. That is, upon photoexcitation or carrier injection electrons and holes accumulate at the sites of their respective parent ionized impurities and compensate their charge. As a result, the superlattice modulation is reduced and the effective energy gap increases.

Doping superlattices were proposed approximately 20 years ago[36,37] in a homogeneously doped configuration. The first δ-doped doping superlattices were grown in 1985.[38] Delta-doped doping superlattices have improved optical properties and made possible the first observation of quantum-confined optical interband transitions in absorption and photoluminescence measurements.[16,17,39]

In the following we discuss experimental results on transmission experiments. Absorption and luminescence spectroscopy which revealed quantum-confined transitions will not be discussed here but were reported in the literature.[16,17] Transmission spectroscopy on δ-doped doping superlattices, using semiconductor diodes to detect the transmitted light, are advantageous due to reduced noise of the signal as compared to (spectrophotometer) absorption measurements. Transmission experiments are carried out with a cooled Ge photodiode, which detects the light transmitted through the doping superlattice. Using phase sensitive *lock-in* technique for the detection, the transmission signal carries little noise.

For the transmission measurements a sample holder with a 1.0 mm diameter hole is used. The Ge photodiode detector is thermally decoupled from the sample holder. The chopping frequency is 313 Hz. For monochromatic illumination of the sample we use a 250W halogen lamp with a double monochromator (HRD 600 Jobin Yvon) incorporating 1200-lines/mm and 600-lines/mm gratings. The holographic 1200-lines/mm grating is used for the measurements due to the smooth optical response. In addition, optical filters with cutoff wavelengths of 665 and 780 are used.

The observed spectra are normalized to a reference measurement performed on a semi-insulating substrate with a thickness of 300 μm. In this way one can obtain transmission spectra without detailed knowledge of the response of the measuring setup. From these corrected curves we obtain the first derivative by numerical differentiation. The transmission spectra and its derivative of a δ-doped doping superlattice is shown in Fig. 18. The bulk band gap energy is indicated by an arrow in Fig. 18. A clear decrease of the transmission signal is observed much below the bulk band gap of GaAs. The decrease of the transmission signal occurs at wavelengths of 1100 nm. The onset of absorption (which is equivalent to a decrease in the transmission signal) is consistent with the reduced energy gap of doping superlattices mentioned earlier. The transmission spectrum shows four shoulders which are identified as quantum-confined interband transitions. The structure is stronger in the derivative of the transmission spectrum.

The transition energies can be calculated using either the exact Airy-function solution[16] or a variational approach.[17] The theoretical transition energies are matched to the transmission peaks by adjusting the two parameters of the doping superlattice (i) period and (ii) doping density. Best agreement between measured and calculated transition energies is obtained, if a period of 142 Å and a doping density of 1.3×10^{13} cm^{-2} is used.

The derivative of the transmission spectrum of a superlattice with longer period and smaller doping density is shown in Fig. 19. The number of peaks has significantly increased in the wavelength interval as compared to the sample shown in Fig. 18. A decrease in doping density leads to a decrease in the subband spacing. More peaks with narrower spacing are

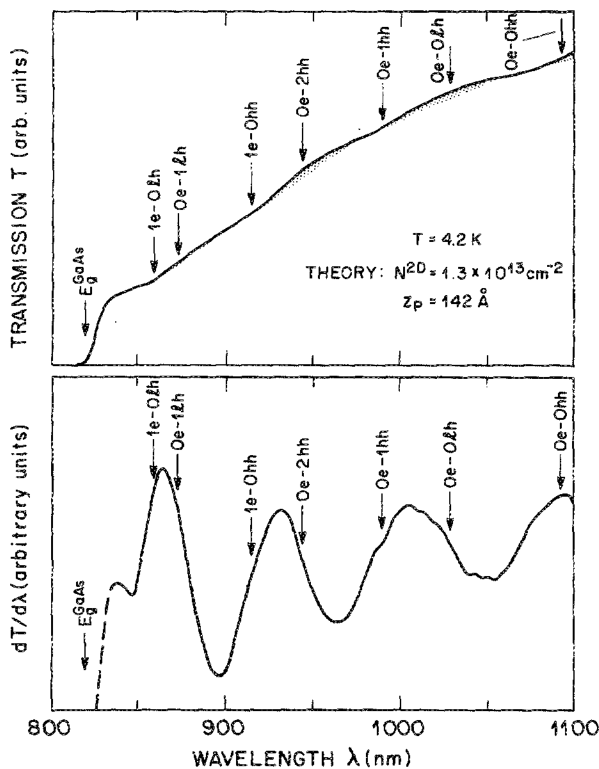

FIG. 18. Transmission and derivative of transmission vs wavelength of a sawtooth doping superlattice at low temperatures. The arrows represent calculated transition wavelengths using the superlattice parameters $N^{2D} = 1.3\times10^{13}$ cm^{-2} and $z_p = 142$ Å.

therefore plausible for superlattices with smaller doping density.

The energies of quantum confined interband transitions are calculated using the exact Airy-function solution. For a period of $z_p = 178$ Å and a doping density of 9×10^{12} cm^{-2} one obtains the theoretical transition energies shown by the arrows in Fig. 19. Good agreement is found between measured and calculated transition energies.

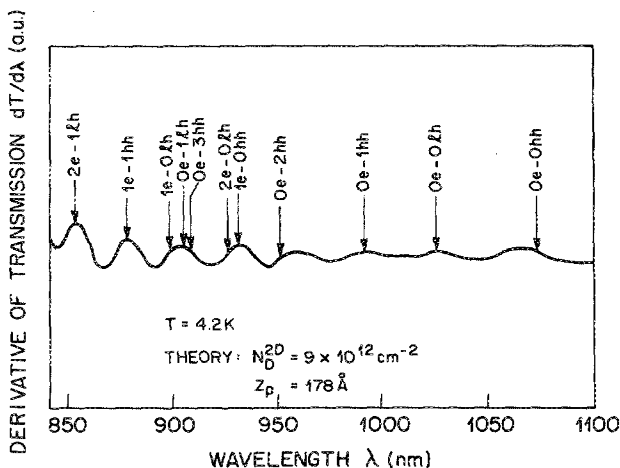

FIG. 19. Derivative of the transmission vs wavelength of a sawtooth doping superlattice at low temperature. The superlattice has a smaller doping density and a longer period as compared to the spectrum shown in Fig. 18. The arrows represent calculated transition wavelengths using the superlattice parameters $N^{2D} = 9\times10^{12}$ cm^{-2} and $z_p = 178$ Å.

The absorption coefficient for one-photon absorption can be obtained in terms of Fermi's Golden Rule

$$\alpha(\omega) = \frac{4\pi e^2}{\omega c n_r m^2} \sum_{n\neq n'} |\langle F|p\epsilon|I\rangle|^2 \delta(\omega - \omega_{nn'}), \qquad (23)$$

where $\langle F|$ and $|I\rangle$ are the final and initial states, p is the dipole operator, c the speed of light, ϵ the polarization of the photon, and n_r the index of refraction. Taking into account the multiple internal reflections within the sample, we write

$$T(\omega) = \frac{(1-R)^2 e^{-\alpha(\omega)t}}{1 - R^2 e^{-2\alpha(\omega)t}}, \qquad (24)$$

where R is the reflectivity given by $R = (n_r - 1)^2/(n+1)^2$ in the long-wavelength limit; t is the thickness of the sample. The estimated order of magnitude of the absorption coefficient for our sample is $\lesssim 1000$ cm^{-1} and so the denominator can be treated as unity. We thus have $T(\omega) = (1-R)^2 e^{-\alpha(\omega)t}$ and can write its derivative with respect to wavelength as

$$\frac{dT(\omega)}{d\lambda} = \frac{tc}{\lambda^2}\frac{d\alpha(\omega)}{d\omega}(1-R)^2 e^{-\alpha(\omega)t}. \qquad (25)$$

The absorption coefficient for a subband transition is a broadened step function and therefore its derivative has a peak when the photon energy is equal to any transition energy and has a dip when the photon energy lies in the middle between two transition energies.

Some properties of doping superlattices make possible semiconductor devices not feasible in other semiconductor systems. Specifically, the reduced superlattice energy gap and the tunability of the gap open intriguing possibilities for device application. The reduced energy gap allows one to extend the wavelength range of light-emitting devices. Thus, GaAs devices can operate at wavelengths $\lambda > 0.9$ μm. The tunability of the energy gap allows one to continuously tune the emission energy of light-emitting diodes or lasers.

Lasers are one of the most interesting device applications for doping superlattices. Tunable lasers are highly desirable for optical wavelength multiplex communication systems. On the other hand, optical transitions in doping superlattices are inherently of weaker oscillator strength as compared to bulk material. Thus, the realization requires high quality epitaxial material.

The first doping superlattice current injection laser[19] was realized in GaAs using the δ-doped technique. The schematic sketch of a current-injection doping superlattice laser is shown in Fig. 20. The laser comprises a doping superlattice region in which radiative recombination occurs. The doping profile and the band diagram is shown in the inset of Fig. 20. The superlattice region is confined by n- and p-type $Al_xGa_{1-x}As$ regions. In addition to current injection lasers, also optically pumped double heterostructure lasers were demonstrated.[20]

The first tunable doping superlattice laser was realized by inhomogeneous optical excitation of the Fabry–Perot cavity.[20] After epitaxial growth, the layers are cleaved into bars of nominal 250 μm width and 1 cm length. A frequency-doubled Nd-doped Q-switched YAG laser ($\lambda = 532$ nm) is used for optical excitation. Light emission from the sample is detected with a Si detector using gated detection. The laser

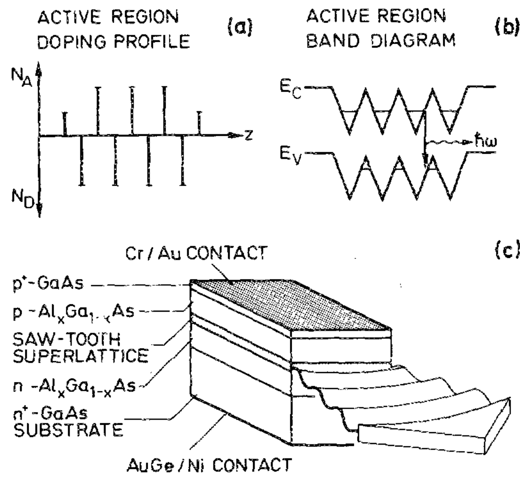

FIG. 20. (a) Doping profile, (b) band diagram, and (c) basic structure of the edge-emitting sawtooth superlattice laser. The active doping superlattice region is sandwiched between $Al_xGa_{1-x}As$ confinement layers.

samples are cooled in a variable-temperature He cryostat.

The transverse electric (TE) and magnetic (TM) emission modes of an optically pumped doping superlattice laser is shown in Fig. 21. The TM polarized spectrum is magnified ($\times 100$) in the illustration. The spectrum of the TE polarized emission shows several longitudinal Fabry–Perot modes of the laser and the absence of spontaneous emission.

The spontaneous and stimulated emission spectra are shown together with the light output versus excitation intensity curve in Fig. 22 for a temperature of 150 K. In the spontaneous emission regime at low excitation intensity the peak wavelength moves to shorter wavelength with increasing excitation intensity. At higher excitation intensities stimulated emission occurs, which is accompanied by the characteristic kink in the light output curve of Fig. 22 and a narrowing of the emission spectrum below values of the thermal energy kT. However, the peak wavelength does not change in the stimulated emission regime as clearly revealed in Fig. 22. Such a constant emission energy is not unexpected, since upon reaching the laser threshold the Fermi level remains constant and additional carriers undergo stimulated recombination with a correspondingly very short lifetime. Thus, the emission energy remains constant with excitation energy in the stimulated emission regime.

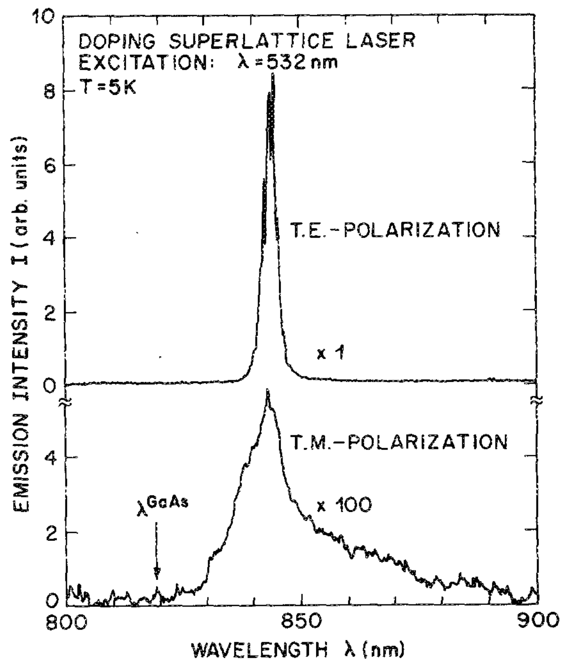

FIG. 21. Spectrum of the doping superlattice laser with transverse electric (TE) and transverse magnetic (TM) polarization. The TE polarization spectrum reveals a number of longitudinal modes.

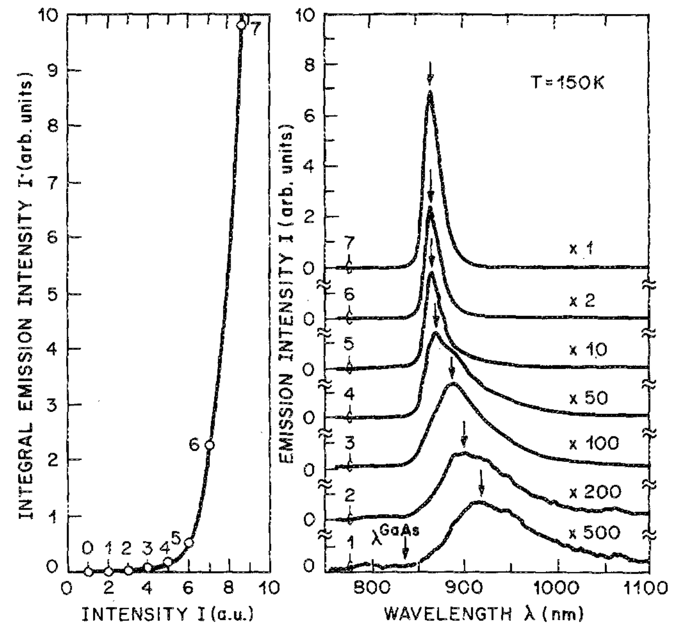

FIG. 22. (Left) Emission intensity vs excitation intensity of the tunable sawtooth superlattice laser at $T \approx 150$ K. (Right) Optical spectra below threshold intensity, at threshold intensity, and above threshold intensity. The laser wavelength remains constant when the stimulated emission threshold is reached.

However, the emission energy can be tuned continuously by inhomogeneous excitation of the Fabry–Perot cavity. Such inhomogeneous excitation is achieved by displacing the exciting optical beam from its centered position, as shown in the top part of Fig. 23. The inhomogeneous excitation results in a laser emission energy higher as compared to the symmetric excitation. Figure 23 reveals that the tuning range of the laser is approximately 35 Å. This tuning range does not represent a fundamental limit. The current tuning range is limited by the intensity distribution of the exciting source. We expect a wider tuning range for a more inhomogeneous excitation, which could be also achieved in a two- or three-section current-injection laser.

Simultaneously, as the peak of the stimulated emission shifts to shorter wavelength, the excitation intensity required to reach threshold increases, as illustrated in Fig. 23(b). However, it is important to visualize that upon displacement, the sample is excited only by a small part of the exciting beam as shown in the inset of Fig. 23. Thus, the increase of threshold intensity is overestimated and the true

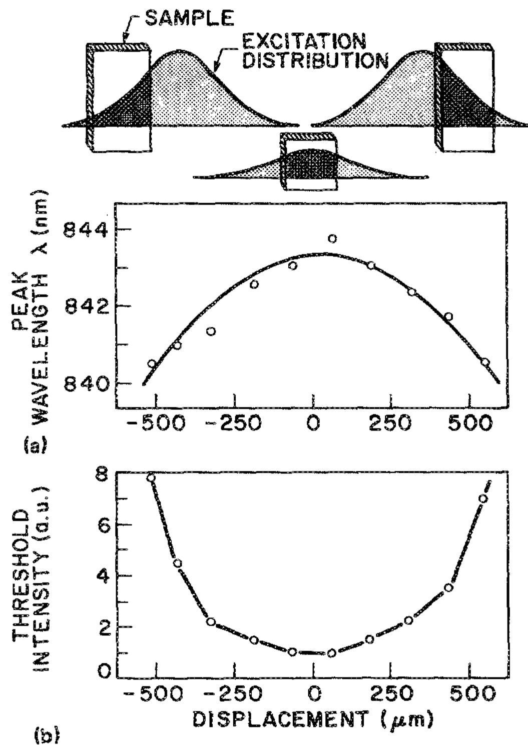

FIG. 23. (a) Peak wavelength of the tunable laser vs displacement of the optical excitation beam. Tunability of the laser emission is achieved over 35 Å. (b) Threshold intensity of the laser vs displacement of the exciting beam. The top part of the figure shows the displacement of the exciting beam with respect to the laser bar.

increase in threshold intensity is not as pronounced as suggested by Fig. 23(b).

Under homogeneous excitation conditions the stimulated emission energy is several 10 meV below the band gap of bulk GaAs. However, the emission energy is much higher than the spontaneous emission energy at low excitation intensities ($E \cong 1.35$ eV). Thus, the superlattice modulation is reduced by photoexcited electrons and holes, which screen the ionized dopant charges of donors and acceptors, respectively. Even though the modulation is reduced, a residual band modulation is still maintained, as suggested by the low emission energy. Thus, stimulated emission is achieved before the bands are completely flat, that is, for incomplete screening of dopant charges.

The physical mechanism leading to the tunability of the semiconductor laser can be understood on the basis of increased loss induced by inhomogeneous excitation. As a result of the inhomogeneous excitation, i.e., reduced excitation intensity in one part of the Fabry–Perot cavity, the optical loss is enhanced in this section. In order to obtain stimulated emission, the other section must be subjected to higher excitation. As a result, the band modulation decreases and the superlattice energy gap increases in this section due to an enhanced density of carriers. Once the intentionally induced loss is overcome, stimulated emission occurs. The corresponding energy is increased as compared to the homogeneously excited cavity. Thus, tunability of the stimulated emission wavelength is achieved by a different excitation in the two sections of the laser. The principal limit of the tuning range is reached when the flatband condition is achieved in one part of the laser. The corresponding tuning range is approximately 250 Å at low temperatures for the samples studied here.

VIII. CONCLUSIONS

Research and development in the field of semiconductor technology has always been focused on the fundamental physical limits such as limits of miniaturization, speed, and integration of electronic and/or optical circuits. The realization of δ-function-like doping distributions represents such a fundamental limit. It was shown in this review what δ-doped semiconductors are, and how they are realized. Furthermore, a number of device applications were reviewed.

The field of δ-doped is a truly interdisciplinary field. It involves (i) materials science, (ii) solid state physics, (iii) quantum mechanics, and (iv) device physics. Contributions from each of these fields are essential to the realization and understanding of δ-doped semiconductors. The interdisciplinary nature of the subject makes the field exciting and filled with a wealth of opportunities.

Employment of the δ-doped technique results in a significant improvement of a number of semiconductor structures and devices. The improved structures include homo and heterostructure field effect transistors and nonalloyed ohmic contacts.[40] For many purposes the δ-function-like doping distribution represents an optimized doping distribution. For example, selectively δ-doped heterostructures have both, highest densities as well as highest mobilities.[35] Novel structures and devices are made possible through the δ-doping technique, including the tunable doping superlattice laser. Future research and development of semiconductors will make use of the advances and the knowledge gained in the course of research in the field of δ doping. Certainly, the intention is the further improvement of semiconductor structures and devices.

However, research on δ-doped semiconductors continues. The employment of δ-function-like doping distributions requires improved crystal growth and processing technology. Many challenges will be met and the physics must be understood, before the development and the production of semiconductor devices can take full advantage of the δ-doping technique. This continues to make the physics of δ-doped semiconductors such an attractive field.

ACKNOWLEDGMENTS

I have greatly benefitted from collaborations with colleagues at AT&T Bell Laboratories. I am grateful to J. E. Cunningham, R. F. Kopf, J. M. Kuo, R. J. Malik, and Loren Pfeiffer, who grew epitaxial crystals of exceptional quality and parameter control and who contributed through suggestions and discussions. The author also wishes to thank D. Deppe, L. C. Feldman, A. M. Glass, T. D. Harris, R. L. Headrick, H. S. Luftman, S. Schmitt-Rink, W. T. Tsang, C. W. Tu, and J. P. van der Ziel, for support, many valuable discussions, and significant contributions to this work.

[1]S. J. Bass, J. Cryst. Growth 47, 613 (1979).
[2]J. V. DiLorenzo, J. Electrochem. Soc. 118, 1645 (1971).

[3]C. E. C. Wood, G. M. Metze, J. D. Berry, and L. F. Eastman, J. Appl. Phys. **51**, 383 (1980).
[4]H. Lee, W. J. Schaff, G. W. Wicks, L. F. Eastman, and A. R. Calawa, Inst. Phys. Conf. Ser. **74**, 321 (1985).
[5]E. F. Schubert, J. B. Stark, B. Ullrich, and J. E. Cunningham, Appl. Phys. Lett. **52**, 1508 (1988).
[6]E. F. Schubert, C. W. Tu, R. F. Kopf, J. M. Kuo, and L. M. Lunardi, Appl. Phys. Lett. **54**, 2592 (1989).
[7]E. F. Schubert, J. M. Kuo, R. F. Kopf, H. S. Luftman, L. C. Hopkins, and N. J. Sauer J. Appl. Phys. **67**, 1969 (1990).
[8]M. Santos, T. Sajoto, A. Zrenner, and M. Shayegan, Appl. Phys. Lett. **53**, 2504 (1988).
[9]C. Webb, Appl. Phys. Lett. **54**, 2091 (1989).
[10]E. F. Schubert and K. Ploog, Jpn. J. Appl. Phys. Lett. **24**, L608 (1985).
[11]E. F. Schubert, J. E. Cunningham, W. T. Tsang, and G. L. Timp, Appl. Phys. Lett. **51**, 1170 (1987).
[12]R. J. Malik, T. R. AuCoin, R. L. Ross, K. Board, C. E. C. Wood, and L. F. Eastman, Electron. Lett. **16**, 836 (1980).
[13]R. J. Malik and S. Dixon, IEEE Electron. Dev. Lett. **3**, 205 (1982).
[14]E. F. Schubert, J. E. Cunningham, and W. T. Tsang, Appl. Phys. Lett. **51**, 817 (1987).
[15]J. N. Baillargeon, K. Y. Cheng, J. Laskar, and J. Kolodzey, Appl. Phys. Lett. **55**, 663 (1989).
[16]E. F. Schubert, B. Ullrich, T. D. Harris, and J. E. Cunningham, Phys. Rev. B **38**, 8305 (1988).
[17]E. F. Schubert, T. D. Harris, J. E. Cunningham, and W. Jan, Phys. Rev. B **39**, 11011 (1989).
[18]E. F. Schubert, A. Fischer, and K. Ploog, Electron. Lett. **21**, 411 (1985).
[19]E. F. Schubert, A. Fischer, Y. Horikoshi, and K. Ploog, Appl. Phys. Lett. **47**, 219 (1985).
[20]E. F. Schubert, J. P. van der Ziel, J. E. Cunningham, and T. D. Harris, Appl. Phys. Lett. **55**, 757 (1989).
[21]E. F. Schubert, J. M. Kuo, and R. F. Kopf, J. Electron. Mater. (to be published).
[22]E. F. Schubert, J. B. Stark, T. H. Chiu, and B. Tell, Appl. Phys. Lett. **53**, 293 (1988).
[23]R. B. Beall, J. B. Clegg, and J. J. Harris, Semiconduct. Sci. Technol. **3**, 612 (1988); see also R. B. Beall, J. J. Harris, J. B. Clegg, J. P. Gowers, B. A. Joyce, J. Castagnè, and V. Welch, in *GaAs and Related Compounds*, edited by J. S. Harris (Institute of Physics, Bristol, 1989).
[24]B. Tuck, *Atomic Diffusion in III–V Semiconductors* (Hilger, Bristol, 1988).
[25]T. H. Chiu, J. E. Cunningham, B. Tell, and E. F. Schubert, J. Appl. Phys. **64**, 1578 (1988).
[26]E. F. Schubert, J. M. Kuo, R. F. Kopf, A. S. Jordan, H. S. Luftman, and L. C. Hopkins, Phys. Rev. 1990, (submitted).
[27]Y. Nanichi and G. L. Pearson, Solid State Electron. **12**, 341 (1969).
[28]E. F. Schubert, A. Fischer, and K. Ploog, IEEE Trans. Electron. Dev. **33**, 625 (1986).
[29]P. L. Hower and G. Bechtel, IEEE Trans. Electron. Dev. **20**, 213 (1973).
[30]D. Delagebeaudeuf and N. T. Linh, IEEE Trans. Electron. Dev. **29**, 955 (1982).
[31]E. F. Schubert, J. E. Cunningham, and W. T. Tsang, Appl. Phys. Lett. **49**, 1729 (1986).
[32]A. Ishibashi, K. Funato, and Y. Mori, Electron. Lett. **24**, 1035 (1988).
[33]S. S. Pei and N. J. Shah, *Introduction to Semiconductor Technology: GaAs and Related Compounds*, edited by C. T. Wang (Wiley, New York, 1989).
[34]J. E. Cunningham, W. T. Tsang, G. Timp, E. F. Schubert, A. M. Chang, and K. Owusu-Sekyere, Phys. Rev. B **37**, 4317 (1988).
[35]E. F. Schubert, Loren Pfeiffer, K. W. West, and A. Izabelle, Appl. Phys. Lett. **54**, 1350 (1989).
[36]L. Esaki and R. Tsu, IBM J. Res. Dev. **14**, 61 (1970).
[37]G. H. Döhler, IEEE J. Quant. Electron. **22**, 1682 (1986).
[38]E. F. Schubert, Y. Horikoshi, and K. Ploog, Phys. Rev. B **32**, 1085 (1985).
[39]E. F. Schubert, T. D. Harris, and J. E. Cunningham, Appl. Phys. Lett. **53**, 2208 (1988).
[40]E. F. Schubert, J. E. Cunningham, W. T. Tsang, and T. H. Chiu, Appl. Phys. Lett. **49**, 292 (1986).